COMPORTEMENT A LA RUPTURE DES ARTERES

S. Avril, A. Romo, F.M. Davis, P. Badel, A. Duprey, J.P. Favre
Centre Ingénierie et Santé, Mines Saint-Etienne
158 cours Fauriel, 42023 Saint-Etienne Cedex. Téléphone : 04 77 42 01 88, Télécopie : 04 77 42 00 00, Adresse électronique : avril@emse.fr,

Mots clés : Anévrysme, aorte, essais de gonflement, rupture, mesure de champs

1. INTRODUCTION

Each year thoracic aneurysms are diagnosed in approximately 15,000 people in the United States and more than 30,000 people in Europe (Clouse 1998). Of this number 50-60% are ascending thoracic aortic aneurysms (ATAA) (Isselbacher 2005).
The study of the mechanical behavior of the human aorta is an important topic. In particular the rupture of the ATAA is an almost unexplored area. It is currently known that ATAA is caused by the remodeling of the arterial wall and its rupture is caused when the stress applied to the aortic wall locally exceeds its capacity to sustain stress (Vorp et al., 2003).
In an attempt to understand the mechanical behavior of the aortic tissue; different authors have performed mechanical tests. Uniaxial tensile tests were performed by (Mohan and Melvin, 1982) on 34 dumbbell healthy descending aortic specimens; concluding that the most reasonable failure theory for aortic tissue was the maximum tensile strain theory. Also performing uniaxial tests, (He and Roach, 1994) showed that aneurysms were less distensible and stiffer than healthy tissues.
Using uniaxial tensile tests to compare healthy tissues with ATAA specimens (Garcia-Herrera et al., 2011) concluded that the age, beyond the age of 35, was the cause of significant decrease of rupture load and elongation at failure. They found no significant differences between the mechanical strength of aneurysms and healthy tissues. In contrast, (Vorp et al., 2003) found a significant decrease in the tensile strength of the ATAA specimens and concluded that its formation was associated with the stiffening and weakening of the aortic wall.
Providing data on the mechanical behavior in the physiological range, (Duprey et al., 2010) found that the aortic wall was significantly anisotropic with the circumferentially oriented samples being stiffer than the axial ones.
The biaxial mechanical behavior of the aortic tissue can be investigated with bulge inflation tests.
Dynamic and quasi-static bulge inflation tests (Mohan and Melvin, 1983) were performed in 16 healthy descending aortas. The failure of the aortic tissue always took place with a tear in the circumferential direction. Similarly, (Marra et al., 2006) performed inflation tests using porcine healthy aortic tissues, showing that the rupture occurs with a crack oriented in the circumferential direction of the artery. More recently (Kim et al., 2012) performed inflation tests using ATAA specimens. Material parameters were identified using the virtual fields method (Grédiac et al., 2006; Avril et al., 2010) and the average Cauchy stress values at which the rupture occurred were derived for all the specimens.
None of the studies mentioned above analyzed locally the rupture of the tissue from its first initiation. Moreover, all these studies derived average stress estimation across the specimens and none were able to show if the rupture initiates at the location of maximum stress or if the rupture was triggered by the existence of weakened parts within the tissue.
Our objective was to address this issue by carrying out full-field measurements in human ATAA specimens tested in a bulge inflation test up to failure. In order to determine the cause and location of the rupture, thickness evolution estimations and local stress distributions were calculated during the inflation of the specimens.

2. METHODS

ATAA specimens were obtained from donor patients who underwent surgical replacement of their ATAA with a synthetic graft. The collection of the aortic tissues was done in accordance with the

guidelines of the Institutional Review Board of the University Hospital Center of Saint-Etienne. Specimens were kept at 4 °C in 0.9% physiological saline solution and testing was completed within 24 hours of tissue harvest (Adham et al. 1996). Table 1 lists the demographic information for the collected ATAA specimens.

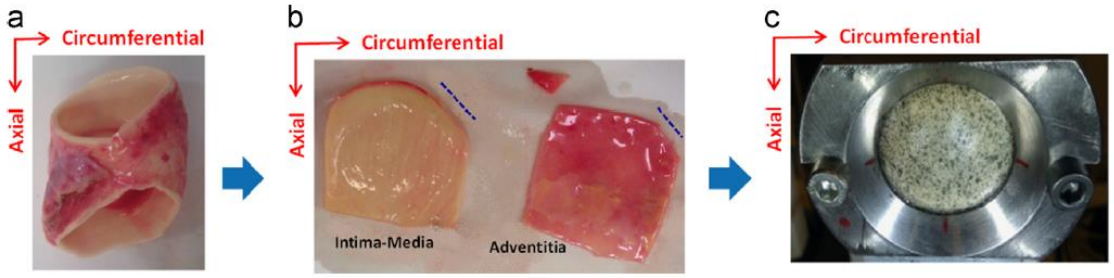

Fig. 1. ATAA specimen preparation for the inflation test.

Table 1
Demographic information for the collected ATAA specimens.

Test no.	Layer type	Sex/age	Diameter before surgery (mm)	*Ex vivo* thickness (mm)
1	Adventitia	M/67	50	1.18
2	Adventitia	M/36	50	0.51
3	Adventitia	M/55	53	0.79
4	Adventitia	M/81	54	0.64
5	Adventitia	M/76	52	0.62
6	Adventitia	M/71	48	0.55
7	Media	M/70	63	0.89
8	Media	M/67	50	0.68
9	Media	M/54	60	0.98
10	Media	M/55	53	1.09
11	Media	F/76	55	1.15
12	Media	M/81	54	0.91
13	Media	M/68	59	1.02
14	Media	M/69	51	1.09
15	Media	M/71	48	1.04

Each ATAA (Fig. 1-a) was cut into square specimen approximately 45 x 45 mm. Each specimen was then separated into two layers: intima-media and adventitia (Fig. 1-b). The average thickness of each layer was measured using a digital caliper; the layer of interest was put between two plastic plates and the thickness of the layer and the plates was measured. Then the thickness of the two plates was subtracted from the value. The ATAA layer was clamped in the inflation device so that the luminal or inner side of the tissue faced outward and the circumferential direction of the artery coincided with the horizontal axis of the clamp (Fig. 1-c). Finally a speckle pattern was applied to each sample using black spray paint (Fig. 1-c). Note that the side of each layer was chosen to face outward since the external surface was highly irregular making difficult for the speckle pattern to adhere to the surface.

A hermetically sealed cavity was formed between the clamped ATAA layer and the inflation device. During the inflation test, water was injected at a constant rate by pushing a piston pump at 15 mm/min until the tissue ruptured. Simultaneously, the pressure was measured with a digital manometer (WIKA®, pressure gauge DG-10). Images were recorded using a commercial DIS-C system (GOM®, ARAMIS 5M LT) at every 3 kPa, until the sample ruptured (Fig. 2). The DIS-C system was composed of two 8-bit CCD cameras equipped with 50 mm lenses (resolution: 1624 x 1236 px). In this study, 15 ATAA layers were successfully tested until rupture. Only the specimens that ruptured in their central area (without touching the boundaries of the inflation device) were used.

Once the experimental procedure was completed, image processing was performed using Aramis® software. In each of the acquired images (Fig. 2), the Area of Interest (AOI), which was a circle measuring 30 mm diameter, was identified. A facet size of 21 px and a facet step of 5 px were chosen based on the speckle pattern dot size, distribution, and contrast. The selected facet size and step yielded a resolution of 0.54 µm for in-plane displacements and 1.5 µm for the out-of-plane displacement.

Based on a technique called stereophotogrammetry, the 2D coordinates captured by both cameras were used to deduce the 3D coordinates of a cloud of points (Fig. 3) across the AOI throughout the test in the global coordinate system (GCS) ($\mathbf{1}$, $\mathbf{2}$, $\mathbf{3}$).

To capture the kinematics of the membrane (Naghdi 1972; Green and Adkins 1970; Lu et al., 2008) we define the position vectors for a material point P in the initial and deformed configurations as $\boldsymbol{X}(P)$ and $\boldsymbol{x}(P)$, respectively (Fig. 4). The surface is parameterized using a pair of surface coordinates

$\xi^{\alpha}(P) = \boldsymbol{X}(P) \cdot \boldsymbol{E}_{\alpha}$ where $\boldsymbol{E}_{\boldsymbol{\alpha}}$ are the vectors of the GCS basis and $\alpha = 1{,}2$.
The local covariant basis vectors $\boldsymbol{g}_{\alpha}$ and $\boldsymbol{G}_{\alpha}$ for the deformed and initial configurations, respectively, are found using the following relationships:

$$\boldsymbol{g}_{\alpha} = \frac{\partial \boldsymbol{x}}{\partial \xi^{\alpha}} \qquad \boldsymbol{G}_{\alpha} = \frac{\partial \boldsymbol{X}}{\partial \xi^{\alpha}} \tag{1}$$

The local contravariant basis vectors $\boldsymbol{g}^{\alpha}$ and $\boldsymbol{G}^{\alpha}$ are then defined as:

$$\boldsymbol{g}^{\alpha} = \frac{\partial \xi^{\alpha}}{\partial \boldsymbol{x}} \qquad \boldsymbol{G}^{\alpha} = \frac{\partial \xi^{\alpha}}{\partial \boldsymbol{X}} \tag{2}$$

The two-dimensional deformation gradient, $\boldsymbol{F}$, is calculated from the current and initial basis vectors:

$$\boldsymbol{F} = \boldsymbol{g}_{\alpha} \otimes \boldsymbol{G}^{\alpha} \tag{3}$$

Then, at each material point, the two- dimensional Green-Lagrange strain is determined:

$$\boldsymbol{E} = \frac{1}{2}(\boldsymbol{F}^{T}\boldsymbol{F} - \boldsymbol{I}) \tag{4}$$

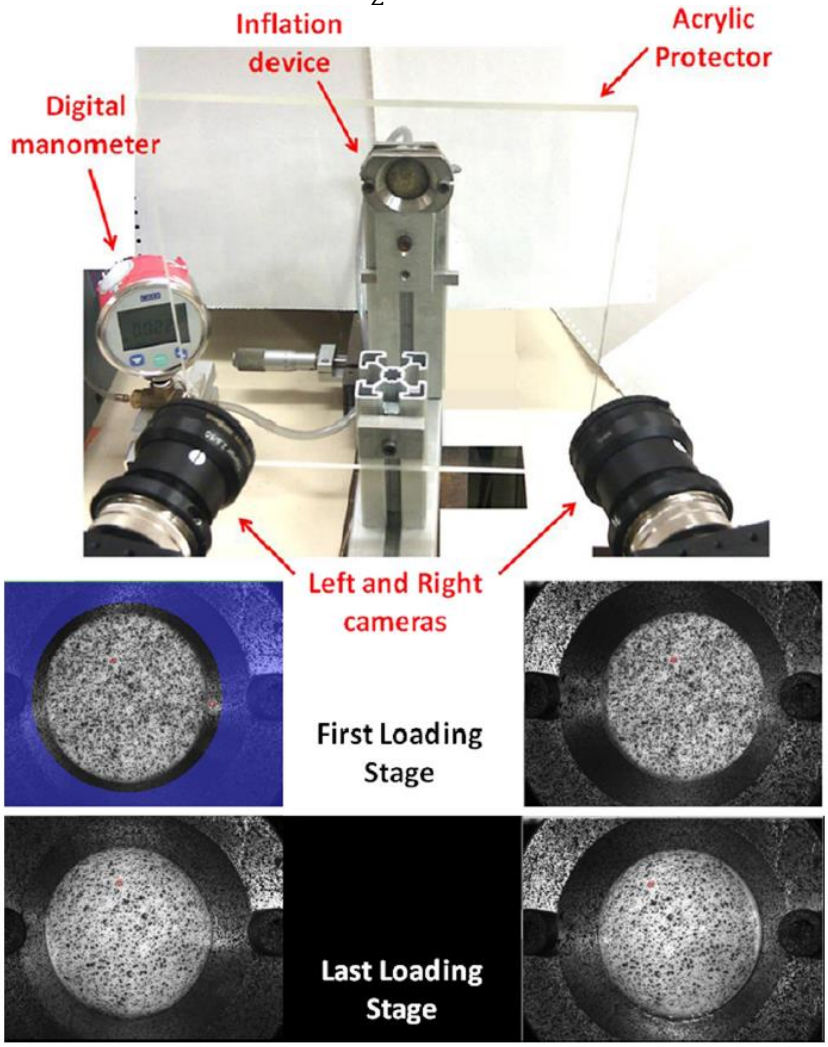

Fig. 2. View of the experimental set-up and the inflation of the ATAA layer through the left and right cameras of the DIS-C system. An image is recorded every loading stage defined at 3 kPa, for the duration of the test. Note that the acrylic protector is used to prevent water from reaching the cameras when the specimen bursts.

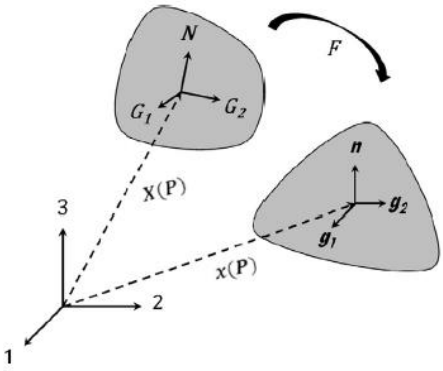

Fig. 3. Schematic of the kinematics and base vectors.

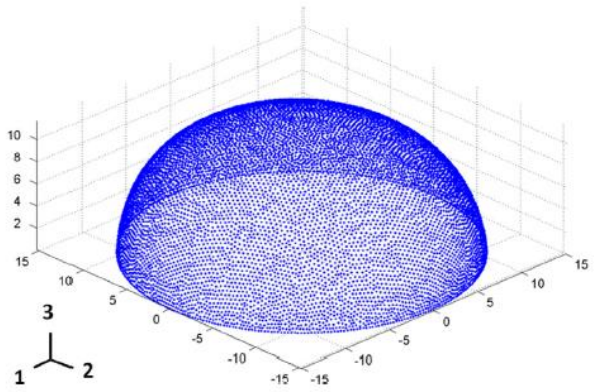

Fig. 4. Reconstructed shape of the ATAA layer at the final inflation stage. The 3D coordinates of each material point were used to reconstruct the shape.

To define the three-dimensional deformation, we set $\lambda_3 = h/h_0$, where h and h_0 are the thicknesses in the deformed and undeformed configurations, respectively, and required the transverse shear strainsto vanish. It follows that the three dimensional deformation gradient and Green-Lagrange strain tensor are given by:

$$\boldsymbol{F} = \boldsymbol{g}_\alpha \otimes \boldsymbol{G}^\alpha + \lambda_3 \boldsymbol{n} \otimes \boldsymbol{N} \qquad \boldsymbol{E} = \frac{1}{2}\left(g_{\alpha\beta}\, \boldsymbol{G}^\alpha \otimes \boldsymbol{G}^\beta + {\lambda_3}^2\, \boldsymbol{N} \otimes \boldsymbol{N} - \boldsymbol{I}\right) \tag{5}$$

where $\boldsymbol{n}$ and $\boldsymbol{N}$ are outward unit normals to the surface in the current and initial configurations, respectively.

The local equilibrium equations for the elastostatic problem may be written as (Naghdi 1972; Lu et al., 2008; Zhao 2009):

$$\frac{1}{\sqrt{g}}\left(\sqrt{g} h \sigma^{\alpha\beta} \boldsymbol{g}_\alpha\right)_{,\beta} + p\boldsymbol{n} = \boldsymbol{0} \tag{6}$$

where $g = \det(\boldsymbol{g}_\alpha . \boldsymbol{g}_\beta)$ is the determinant of the metric tensor, h is the current thickness, p is the internal pressure applied for the inflation and $\sigma^{\alpha\beta}$ are the components of the Cauchy stress tensor $\boldsymbol{\sigma}$ in the local covariant basis.

Then, we approximate the spatial variations of all the quantities of Eq. 6 such as:

$$\begin{aligned}
&\sqrt{g(\boldsymbol{x})} h(\boldsymbol{x}) \sigma^{\alpha\beta}(\boldsymbol{x}) \boldsymbol{g}_\alpha(\boldsymbol{x}) \\
&= \sum_k \left[\sqrt{g(\boldsymbol{x_k})} h(\boldsymbol{x_k}) \sigma^{\alpha\beta}(\boldsymbol{x_k}) \boldsymbol{g}_\alpha(\boldsymbol{x_k})\right] \varphi_k(\xi^1, \xi^2) \\
&\sigma^{\alpha\beta}(\boldsymbol{x}) = \sum_k \sigma^{\alpha\beta}(\boldsymbol{x_k}) \varphi_k(\xi^1, \xi^2) \\
&\boldsymbol{n}(\boldsymbol{x}) = \sum_k \boldsymbol{n}(\boldsymbol{x_k}) \varphi_k(\xi^1, \xi^2) \\
&\sqrt{g(\boldsymbol{x})} = \sum_k \sqrt{g(\boldsymbol{x_k})} \varphi_k(\xi^1, \xi^2)
\end{aligned} \tag{7}$$

where $\boldsymbol{x_k}$ is the current position vector of node k in the mesh and $\varphi_k(\xi^1, \xi^2)$ is a linear shape function of the surface coordinates which takes on a null value at all nodes of the mesh except at node k where it is 1. The shape functions are defined on a triangular finite element mesh having N elements and nodes (Fig. 5).

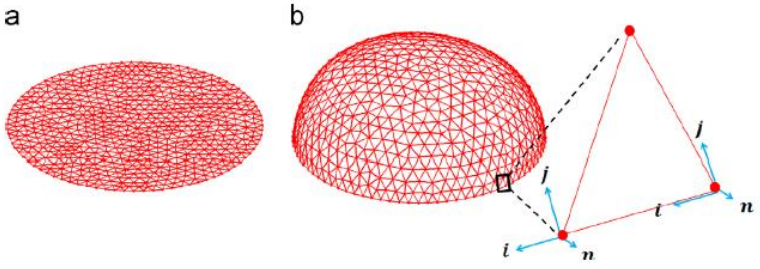

Fig. 5. Discretization of the surface. The unchanged mesh is deformed from (a) the initial to (b) the current configuration. For one boundary element the local (i,j,n) Cartesian frame used to define the boundary conditions is shown.

Using this approximation scheme, Eq. (6) is written at the centroid of each element of the mesh. A linear system of 3N equations is produced. It contains $3K$ unknowns which are the 3 components of the Cauchy stress tensor in the local covariant basis at the K nodes of the mesh.
A convergence study showed that a mesh with N=1203 elements and K=644 nodes was a good compromise between precision and time of calculation.
The system was completed by a set of equations on the boundaries of the tested area, where it was assumed:

$$(\boldsymbol{\sigma} \cdot \boldsymbol{j}) \cdot \boldsymbol{n} = 0 \quad (8)$$

$$(\boldsymbol{\sigma} \cdot \boldsymbol{j}) \cdot \boldsymbol{i} = 0 \quad (9)$$

where $\boldsymbol{i}, \boldsymbol{j}, \boldsymbol{n}$ defines at the boundaries a local basis (Fig. 5-b) with $\boldsymbol{i}$ tangent to the boundary, $\boldsymbol{n}$ outward unit normal vector to the surface and $\boldsymbol{j} = \boldsymbol{n} \otimes \boldsymbol{i}$.
Along the boundaries, Eq. (8) sets that the traction vector was perpendicular to $\boldsymbol{n}$ (in-plane traction vector) and Eq. (9) sets that the traction was perpendicular to $\boldsymbol{i}$ (no shear along this boundary).
The resultant boundary traction automatically balances the total pressure applied on the wall due to the local equilibrium equation (Eq. (6)) written for each element. The final over-determined linear system of equations was solved in the least-squares sense.
The stress was analyzed at three locations:

- NodeMAX: node with the largest stress eigenvalue
- NodeTOP: node at the top of the inflated membrane
- NodeRUP: node where rupture initiates

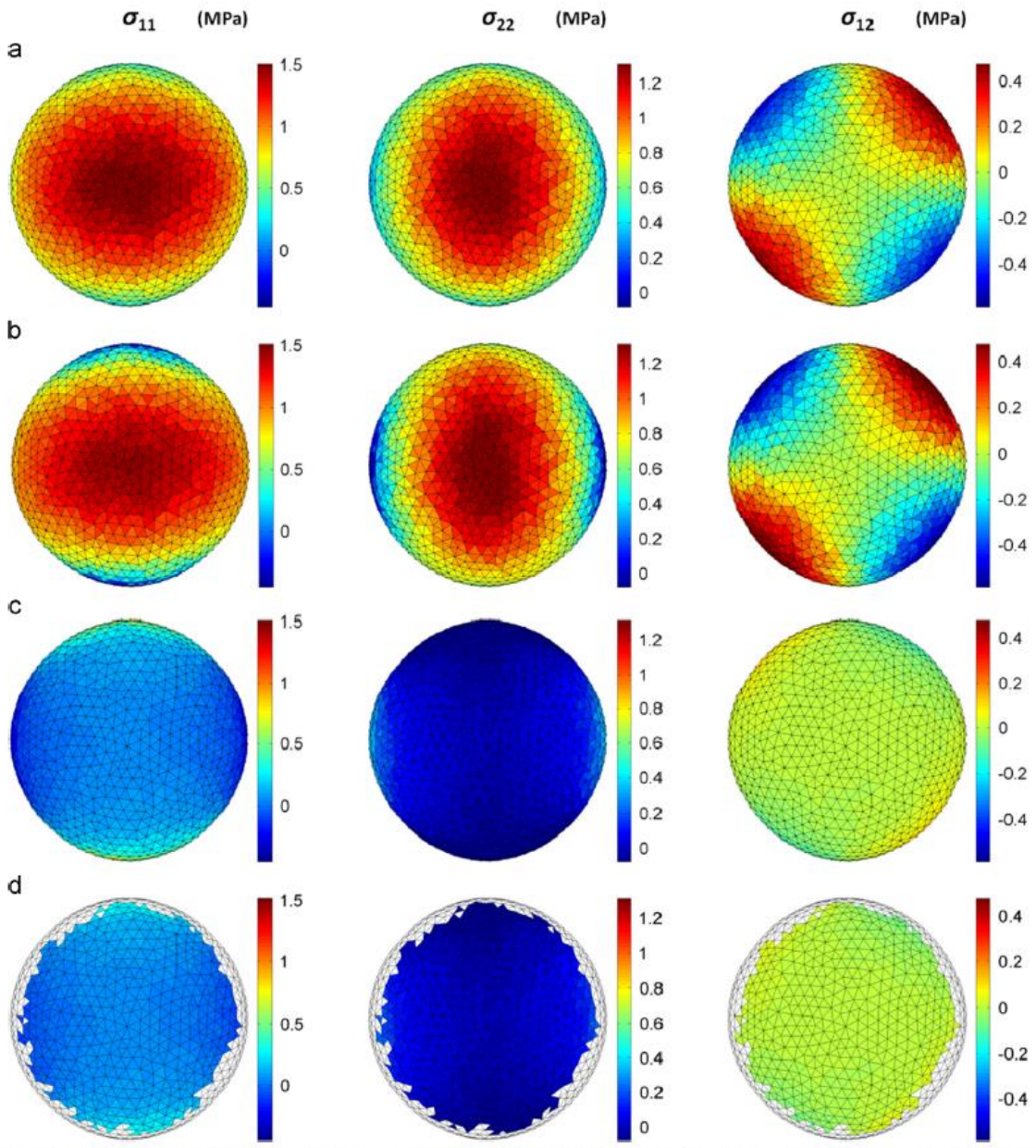

Fig. 6. Top view of the element by element comparison between stress fields calculated by (a) the FEA simulation (reference) and (b) our approach. The absolute error (in MPa) between (a) and (b) is presented in (c) and in (d) where the boundary elements are neglected.

At NodeMAX and NodeTOP locations, the largest eigenvalue of the Cauchy stress tensor (largest principal stress) were found and denoted σ^{Max} and σ^{Top}, respectively. At NodeRUP, the stress in the direction perpendicular to the crack that occurs at rupture was computed:

$$\sigma^{Rup} = (\boldsymbol{\sigma} \cdot \boldsymbol{q_\theta}) \cdot \boldsymbol{q_\theta} \tag{10}$$

where $\boldsymbol{q_\theta}$ is the unit vector perpendicular to the crack. It is derived for each specimen using the images obtained from the DIS-C system at the moment of the rupture. Using a custom Matlab® code, a series of points were manually placed on an image of the ruptured edge. A linear regression was then performed using those points and the angle between the fit line and the circumferential orientation (horizontal axis) was calculated.

At every pressure step, the current thickness of each element was calculated. The aneurysmal tissue was modeled as incompressible membrane therefore the following relationship holds between the initial thickness, h_0, and the current thickness, h.

$$h = \frac{h_0}{F_{11}F_{22} - F_{21}F_{12}} \tag{12}$$

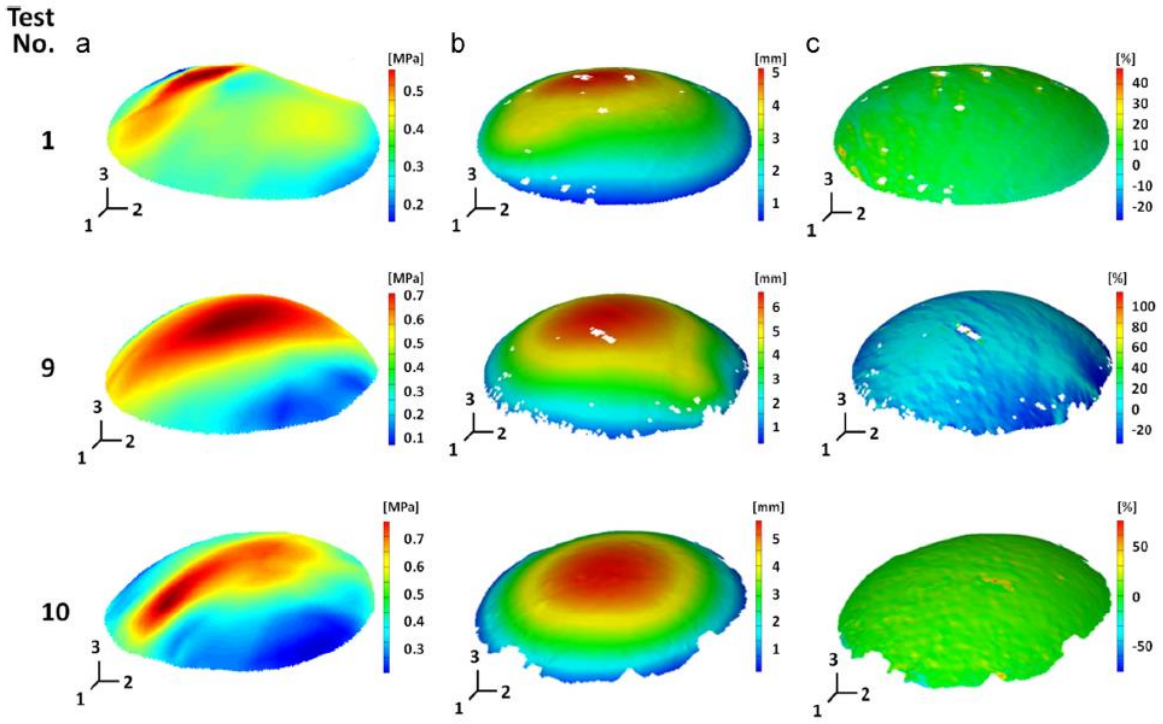

Fig. 7. The (a) stress field (σ_{11}), (b) displacement field (U_3) and (c) strain field (E_{22}) for three ATAA specimens all at a pressure of 0.027 MPa.

We note that the *ex vivo* thickness, h_0, was assumed to be initially homogeneous and that F_{11}, F_{22}, F_{21} and F_{12} were the components of the deformation gradient tensor (Eq. (3)).

Laplace's Law (Peterson et al., 1960; Humphrey 2002) was used to calculate a global estimate of the ultimate stress for each ATAA layer by assuming the sample was a hemisphere.

$$\sigma^{Lap} = \frac{pr}{2h} \tag{13}$$

where p was the inflation pressure, r was the radius of curvature estimated using a least-squares surface fitting of the inflated shape, and h was the average current thickness of the elements in the mesh.

Table 2
Components of the Cauchy stress tensor reported at the NodeMAX, NodeTOP and NodeRUP locations (in MPa). Test No. 1 to 6 were adventitia layers and Test No. 7 to 15 were media layers.

Test no.	NodeMAX			NodeTOP			NodeRUP		
	σ_{11}	σ_{22}	σ_{12}	σ_{11}	σ_{22}	σ_{12}	σ_{11}	σ_{22}	σ_{12}
1	1.124	1.091	−0.036	0.681	0.842	−0.098	1.128	1.062	−0.005
2	3.066	3.812	−0.065	3.035	3.778	−0.064	2.954	3.527	0.084
3	1.233	1.613	−0.011	1.246	1.554	0.023	0.977	0.949	0.189
4	0.938	0.853	0.001	0.922	0.863	−0.002	0.922	0.795	0.012
5	1.964	1.642	0.050	1.920	1.647	0.020	1.699	1.419	−0.042
6	1.035	1.019	−0.046	1.035	1.019	−0.046	0.920	0.933	−0.108
7	0.756	0.997	0.041	0.677	0.909	0.078	0.640	0.924	0.006
8	1.764	1.654	0.097	1.617	1.573	0.077	1.120	0.913	−0.051
9	1.042	1.064	−0.06	1.033	1.067	−0.05	0.903	1.049	−0.027
10	1.308	1.007	−0.012	1.042	1.038	−0.028	1.174	0.927	−0.042
11	0.627	0.622	−0.009	0.549	0.602	−0.03	0.552	0.605	−0.025
12	0.631	0.630	0.076	0.664	0.633	0.042	0.655	0.626	0.040
13	0.819	0.720	−0.055	0.805	0.714	−0.053	0.815	0.725	−0.051
14	0.728	0.866	−0.018	0.800	0.858	−0.016	0.791	0.805	0.0001
15	0.805	0.601	−0.037	0.79	0.588	−0.044	0.714	0.546	−0.041
Mean	**1.18**	**1.21**	**−0.006**	**1.12**	**1.17**	**−0.013**	**1.06**	**1.05**	**−0.004**
Std.	**0.64**	**0.80**	**0.05**	**0.64**	**0.79**	**0.05**	**0.59**	**0.71**	**0.06**

3. RESULTS

Using the approach we have presented, the components of the Cauchy stress tensor were calculated at every node for each 3 kPa pressure step until the sample ruptures (Fig. 6-a). The displacement (Fig. 6-b) and strain fields (Fig. 6-c) used to calculate the stress and thickness evolution are also shown.

In Table 2 we report the three components of the Cauchy stress tensor. Our results (mean ± std) in the circumferential direction (σ_{11}) were 1.18 ±0.64 MPa at NodeMAX, 1.12 ±0.64 MPa at NodeTOP and 1.06 ±0.59 MPa at NodeRUP. The values for the axial direction (σ_{22}) were 1.21 ±0.80 MPa at NodeMAX, 1.17 ±0.79 MPa at NodeTOP and 1.05 ±0.71 MPa at NodeRUP.

In Fig. 7-a, we show the thickness distribution (Eq. (12)) one pressure step before rupture for five tests. For each of the samples thick (dark red) and thin (dark blue) regions can be identified. The locations of NodeMAX, NodeTOP, and NodeRUP for these five tests are also shown in Fig. 7-b. Contrary to the common idea that the rupture occurs at the location of the maximum stress, it was evidenced that rupture often initiates at a different location (NodeRUP), possibly due to the non-homogeneous strength of the tissue. An image of the ruptured layer is shown in Fig. 7-c, where the magenta points and the blue regression line were used to determine the rupture angle θ.

Table 3 and Fig. 8 summarizes the three ultimate stress values (σ^{Max}, σ^{Top}, and σ^{Rup}) calculated at their corresponding locations (NodeMAX, NodeTOP and NodeRUP) compared with σ^{Lap} (Eq. (13)). For the six adventitia layers, the average stress values (mean ± std) were 1.49 ±1.06 MPa, 1.76 ±1.07 MPa, 1.69 ±1.10 MPa, and 1.46 ±1.03 MPa for σ^{Lap}, σ^{Max}, σ^{Top}, and σ^{Rup}, respectively. For the remaining nine media layers, the average stress values were found to be 0.78 ±0.26 MPa, 1.01 ±0.36 MPa, 0.95 ±0.31 MPa, and 0.78 ±0.20 MPa for σ^{Lap}, σ^{Max}, σ^{Top}, and σ^{Rup}, respectively. The four calculated ultimate stress values were higher for the adventitia layers, confirming its role of structural support of the artery (Fung, 1993).

4. CONCLUSION

Our results showed that rupture in the ATAA inflated layers was more prone to occur in regions where the layer was weakened. In most of the cases, rupture occurs where the thickness of the layer has been reduced the most. Visualizing the thickness evolution of the layer can easily predict the localization of the rupture. In a future work this approach could be used *in vivo* to track the stress distribution in real aneurysms using magnetic resonance imaging. It could be used to help clinicians to define a patient-specific criterion for the risk of aneurysm rupture.

4. ACKNOWLEDGEMENT

The authors would like to acknowledge the National Council on Science and Technology of Mexico (CONACYT) for funding Dr. Romo's scholarship. The authors are also grateful to the European Research Council for grant ERC-2014-CoG BIOLOCHANICS.

4. REFERENCES

V. Agrawal, S. A. Kollimada, A. G. Byju, N. Gundiah. Regional variations in the nonlinearity and anisotropy of bovine aortic elastin. *Biomechanics and Modeling in Mechanobiology*, **12**(6), pp. 1181-1094, 2013.

S. Avril, M. Bonnet, A.-S. Bretelle, M. Grédiac, F. Hild, P. Ienny, F. Latourte, D. Lemosse, S. Pagano, E. Pagnacco, F. Pierron. Identification from measurements of mechanical fields. *Experimental Mechanics*, **48**(5), pp. 381-402, 2008.

F. Cuomo, J. Ferruzzi, J.D. Humphrey, A. Figueroa Alvarez. An Experimental–Computational Study of Catheter Induced Alterations in Pulse Wave Velocity in Anesthetized Mice. *Annals of Biomedical Engineering*, in press. 2015

S. Avril, P. Badel, A. Duprey. Anisotropic and hyperelastic identification of in vitro human arteries from full-field measurements. *Journal of Biomechanics*, **43**(15), pp. 2978-2985, 2010.

C. Bellini, J. Ferruzzi, S. Roccabianca, E. S. Di Martino, J. D. Humphrey. A microstructurally motivated model of arterial wall mechanics with mechanobiological implications. *Annals of Biomedical Engineering*, **42**(3), pp. 488-502, 2014.

M. Bersi, M. J. Collins, E. Wilson, J. D. Humphrey. Disparate changes in the mechanical properties of murine carotid arteries and aorta in response to chronic infusion of angiotensin-II. *International Journal of Advances in Engineering Sciences and Applied Mathematics*, **4**(4), pp. 228-240, 2012.

J. Ferruzzi, D. A. Vorp, J. D. Humprey. On constitutive descriptors of the biaxial mechanical behaviour of human abdominal aorta and aneurysms. *Journal of the Royal Society Interface*, **8**(56), pp. 435-450, 2011.

J. Ferruzzi, M. R. Bersi, S. Uman, H. Yanagisawa, J. D. Humphrey. Decreased elastic energy storage, not increased material stiffness, characterizes central artery dysfunction in fibulin-5 deficiency independent of sex. *Journal of Biomechanical Engineering*, **137**(3), pp. 031007-1,14, 2014.

C. M. García-Herrera, D. J. Celentano, M. Cruchaga, F. J. Rojo, J. M. Atienza, G. V. Guinea, J. M. Goicolea. Mechanical characterisation of the human thoracic descending aorta: experiments and modelling. *Computer Methods in Biomechanics and Biomedical Engineering*, **15**(2), pp. 185-193, 2012.

K. Genovese. A video-optical system for time-resolved whole-body measurement on vascular segments. *Optics and Lasers in Engineering*, **47**, pp. 995-1008, 2009.

K. Genovese, Y. U. Lee, J. D. Humphrey. Novel optical system for in vitro quantification of full surface strain fields in small arteries: I. Theory and design. *Computer Methods in Biomechanics and Biomedical Engineering*, **14**(3), pp. 213-225, 2011.

K. Genovese, Y. U. Lee, J. D. Humphrey. Novel optical system for in vitro quantification of full surface strain fields in small arteries: II. Correction for refraction and illustrative results. *Computer Methods in Biomechanics and Biomedical Engineering*, **14**(3), pp. 227-237, 2011.

K. Genovese, Y. U. Lee, A. Y. Lee, J. D. Humphrey. An improved panoramic digital image correlation method for vascular strain analysis and material characterization. *Journal of the Mechanical Behavior of Biomedical Materials*, **27**, pp. 132-142, 2013.

R. L. Gleason, S. P. Gray, E. Wilson, J. D. Humphrey. A multiaxial computer-controlled organ culture and biomechanical device for mouse carotid arteries, *Journal of Biomechanical Engineering*, **126**(6), pp. 787-795, 2004.

G. A. Holzapfel, T. C. Gasser, R. W. Ogden. A new constitutive framework for arterial wall mechanics and a comparative study of material models. *Journal of Elasticity*, **61**, pp. 1-48, 2000.

L. Horný, M. Netušil, T. Voňavková. Axial prestretch and circumferential distensibility in biomechanics of abdominal aorta. *Biomechanics and Modeling in Mechanobiology*, **13**(4), pp. 783-799, 2014.

J. D. Humphrey. *Cardiovascular Solid Mechanics: Cells, Tissues, and Organs*. New York: Springer, 757 pp, 2002.

J. D. Humphrey, J. F. Eberth, W. W. Dye, R. L. Gleason. Fundamental role of axial stress in compensatory adaptations by arteries. *Journal of Biomechanics*, **42**, pp. 1-8, 2009.

HC Han. A biomechanical model of artery buckling. *Journal of Biomechanics*, **40**, pp. 3672-3678, 2007.

A. V. Kamenskiy, Y. A. Dzenis, S. A. Kazmi, M. A. Pemberton, I. I. Pipinos, N. Y. Phillips, K. Herber, T. Woodford, R. E. Bowen, C. S. Lomneth, J. N. MacTaggart. Biaxial mechanical properties of the human thoracic and abdominal aorta, common carotid, subclavian, renal and common iliac arteries. *Biomechanics and Modeling in Mechanobiology*, **13**(2), pp. 1341-1359, 2014.

E. Kuhl, R. Maas, G. Himpel, A. Menzel. Computational modeling of arterial wall growth. Attempts towards patient-specific simulations based on computer tomography. *Biomechanics and Modeling in Mechanobiology*, **6**(5), pp. 321-331, 2007.

V. P. Le, Y. Yamashiro, H. Yanagisawa, J. E. Wagenseil. Measuring, reversing, and modeling the mechanical changes due to the absence of Fibulin-4 in mouse arteries. *Biomechanics and Modeling in Mechanobiology*, **13**(5), pp. 1081-1095, 2014.

A. Maier, M. W. Gee, C. Reeps, H. H. Eckstein, W. A. Wall. Impact of calcifications on patient-specific wall stress analysis of abdominal aortic aneurysms. *Biomechanics and Modeling in Mechanobiology*, **9**(5), pp. 511-521, 2010.

G. Martufi, T.C. Gasser, J.J. Appoo, E.S. Di Martino. Mechano-biology in the thoracic aortic aneurysm: a review and case study. *Biomechanics and Modeling in Mechanobiology*. **13**(5), pp. 917-928, 2014.

P. Moireau, N. Xiao, M. Astorino, C.A. Figueroa, D. Chapelle, C.A. Taylor, J.F. Gerbeau. External tissue support and fluid–structure simulation in blood flows. *Biomechanics and Modeling in Mechanobiology*. **11**(1-2), pp. 1-18, 2012.

A. Nahas, M. Bauer, S. Roux, A. C. Boccara. 3D static elastography at the micrometer scale using full-field OCT. *Biomedical Optics Express*, **4**(10), pp. 2138-2149, 2013.

F. Pierron, M. Grédiac. The virtual fields method, New York: Springer, 536 pp, 2012.

A. Podoleanu, I. Charalambous, L. Plesea, A. Dogariu, R. Rosen. Correction of distortions in optical coherence tomography imaging of the eye. *Physics in Medicine and Biology*, **49**(7), pp. 1277-1294, 2004.

C. Reeps, A. Maier, J. Pelisek, F. Härtl, V. Grabher-Meier, W. A. Wall, M. Essler, H. H. Eckstein, M. W. W. Gee. Measuring and modeling patient-specific distributions of material properties in abdominal aortic aneurysm wall. *Biomechanics and Modeling in Mechanobiology*, **12**(2), pp. 717-733, 2013.

S. Roccabianca, C. A. Figueroa, G. Tellides, J. D. Humphrey. Quantification of regional differences in aortic stiffness in the aging human. *Journal of the Mechanical Behavior of Biomedical Materials*, **29**, pp. 618-634, 2014.

S. Roccabianca, G. A. Ateshian, J. D. Humphrey. Biomechanical roles of medial pooling of glycosaminoglycans in thoracic aortic dissection. *Biomechanics and Modeling in Mechanobiology*, **13**(1), pp. 13-25, 2014.

A. J. Schriefl, M. J. Collins, D. M. Pierce, G. A. Holzapfel, L. E. Niklason, J. D. Humphrey. Remodeling of intramural thrombus and collagen in an Ang-II infusion ApoE−/− model of dissecting aortic aneurysms. *Thrombosis Research*, **130**, pp. 139-146, 2012.

M. Smoljkić, J. Vander Sloten, P. Segers, N. Famaey. Non-invasive, energy-based assessment of patient-specific material properties of arterial tissue. *Biomechanics and Modeling in Mechanobiology*, 2015. (Epub ahead of print)

J. Stålhand, A. Klarbring. Aorta in vivo parameter identification using an axial force constraint. *Biomechanics and Modeling in Mechanobiology*, **3**, pp 191-199, 2005.

J. Stålhand. Determination of human arterial wall parameters from clinical data. *Biomechanics and Modeling in Mechanobiology*, **8**(2), pp. 141-148, 2009.

Z. Tonar, P. Kochova, R. Cimrman, J. Perktold, K. Witter. Segmental differences in the orientation of smooth muscle cells in the tunica media of porcine aortae. Determination of human arterial wall parameters from clinical data. *Biomechanics and Modeling in Mechanobiology*, 2014. (Epub ahead of print)

J. P. Van de Geest, M.S. Sacks, D.A. Vorp, Age dependency of the biaxial biomechanical behavior of human abdominal aorta. *Journal of Biomechanical Engineering*, **126**(6), pp. 815–822, 2004.

P. N. Watton, N. A. Hill. Evolving mechanical properties of a model of abdominal aortic aneurysm. Determination of human arterial wall parameters from clinical data. *Biomechanics and Modeling in Mechanobiology*, **8**(1), pp. 25-42, 2009.

V. Westphal, A. M. Rollins, S. Radhakrishnan, J. A. Izatt. Correction of geometric and refractive image distortions in optical coherence tomography applying Fermat's principle. *Optics Express*, **10**(9), pp 397-404, 2002.

J. S. Wilson, S. Baek, J. D. Humphrey. Parametric study of effects of collagen turnover on the natural history of abdominal aortic aneurysms. *Proceedings of the Royal Society of London A*, **469**(2150), 2012.

S. Zeinali-Davarani, L. G. Raguin, D. A. Vorp, S. Baek. Identification of in vivo material and geometric parameters of a human aorta: toward patient specific modeling of abdominal aortic aneurysm. Determination of human arterial wall parameters from clinical data. *Biomechanics and Modeling in Mechanobiology*, **49**(5), pp. 689-699, 2011.

M. Zidi, E. Allaire. Mechanical behavior of abdominal aorta aneurysm in rat model treated by cell therapy using mesenchymal stem cells. *Biomechanics and Modeling in Mechanobiology*, **14**(1), pp. 185-194, 2015.